

# Beyond the blur: using experimental point spread functions to help scanning Kelvin probe microscopy reach its full potential

Isaac C.D. Lenton\*,<sup>1</sup> Felix Perl,<sup>1</sup> Lubuna Shafeek,<sup>1</sup> and Scott R. Waitukaitis<sup>1</sup>

<sup>1</sup>*Institute of Science and Technology Austria, Am Campus 1, 3400 Klosterneuburg, Austria*

(\*Electronic mail: isaac.lenton@ist.ac.at)

(Dated: 23 April 2024)

Scanning Kelvin probe microscopy (SKPM) is a powerful technique for investigating the electrostatic properties of material surfaces, enabling the imaging of variations in work function, topology, surface charge density, or combinations thereof. Regardless of the underlying signal source, SKPM results in a voltage image which is spatially distorted due to the finite size of the probe, long-range electrostatic interactions, mechanical and electrical noise, and the finite response time of the electronics. In order to recover the underlying signal, it is necessary to deconvolve the measurement with an appropriate point spread function (PSF) that accounts the aforementioned distortions, but determining this PSF is difficult. Here we describe how such PSFs can be determined experimentally, and show how they can be used to recover the underlying information of interest. We first consider the physical principles that enable SKPM, and discuss how these affect the system PSF. We then show how one can experimentally measure PSFs by looking at well defined features, and that these compare well to simulated PSFs, provided scans are performed extremely slowly and carefully. Next, we work at realistic scan speeds, and show that the idealised PSFs fail to capture temporal distortions in the scan direction. While simulating PSFs for these situations would be quite challenging, we show that measuring PSFs with similar scan parameters works well. Our approach clarifies the basic principles of and inherent challenges to SKPM measurements, and gives practical methods to improve results.

**This is a pre-print. The following article has been submitted to Journal of Applied Physics. Please check for corrections/modifications when the article is published.**

## I. INTRODUCTION

SKPM enables imaging of the “invisible” electrostatic properties of surfaces at the mesoscale (typically  $>100\text{ }\mu\text{m}$ ). By scanning a vibrating conductive probe above a surface and measuring/regulating the current induced within it (Fig. 1a), SKPM extracts information connected to the local electric potential<sup>1,2</sup>. This gives insight into various processes such as variations in work function or surface chemistry<sup>3,4</sup>, charge<sup>5,6</sup>, biological double layers<sup>7,8</sup>, *etc.* Though not identical, the operating principle behind SKPM is related to Kelvin probe force microscopy (KPFM)<sup>9</sup>, where measurement/regulation of the forces acting on a vibrating atomic force microscope tip permits similar imaging at the nanoscale<sup>10,11</sup>.

A fundamental problem in both SKPM and KPFM is properly interpreting and analyzing the measured signal. Regardless of the signal source (*e.g.* work function variations or charge), both techniques produce voltage images. Moreover, these images are spatially distorted due to the finite size of the probe, long-range electrostatic interactions<sup>12,13</sup>, mechanical and electrical noise<sup>14</sup>, and the temporal response of the electronics<sup>2,15,16</sup>. When these distortions are deterministic and linear, they can be characterised by a PSF, which describes the image an infinitesimally small point in the absence of noise would produce when measured. Effectively, the measured signal is the convolution of the underlying signal with the PSF, and the underlying signal can be recovered by deconvolution<sup>12,13</sup>. Therefore, a key component in interpreting/analyzing SKPM (or KPFM) data relies on being able to determine the PSF that characterises the measurement process.

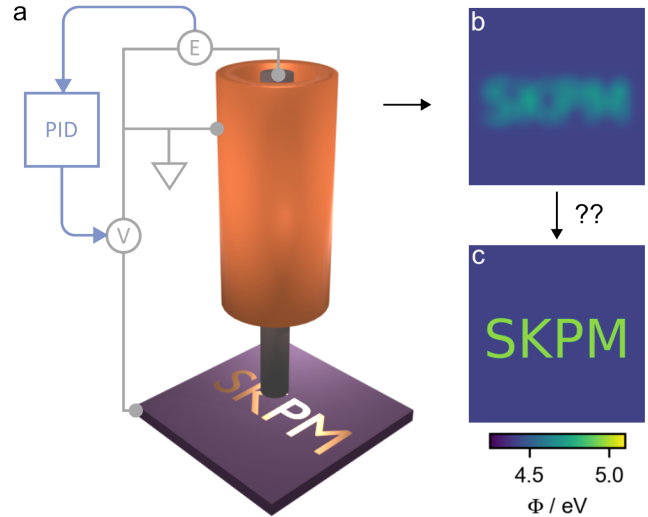


**FIG. 1. Principle of scanning Kelvin probe microscopy (SKPM).** **a** SKPM entails scanning a conductive probe above a sample to estimate the local surface potential. The cylindrical metal probe is vibrated vertically, while a lock-in amplifier and PID use feedback to adjust the backing potential,  $V$ , so that the current in the probe is minimised. **b** Voltage maps measured by SKPM are spatially distorted, due to the probe’s finite size, long-range electrostatics, and the temporal response of the electronics. **c** This paper is about extracting the true underlying surface potential from the measured signal, which we show is achievable by experimentally measuring the system’s PSF and using this to deconvolve raw measurements.

Toward addressing the problem, one can draw inspiration

from optical microscopy. Like SKPM, optical images suffer from distortions, due to diffraction, optical imperfections, finite pixel sizes *etc.* To correct for these, a practical solution is to image the pattern created by a point-like emitter, *e.g.* a small fluorescent particle<sup>17</sup>. When this target is significantly smaller than the system resolution, the image rendered is approximately the PSF.

Here, we show that the approach of experimentally measuring PSFs is not only viable, but effective and straightforwardly implemented in the case of SKPM. We restrict ourselves to the situation where the underlying signal is due to differences in material work functions on a planar surface, though in principle our ideas can be extended to other situations (*e.g.* variations in surface charge). We use common clean-room techniques to pattern regions with work function differences, which we image to extract PSFs. We find that when utilizing high scan speeds—which are necessary to probe large features—the measured PSFs can differ significantly from those that only account for the electrostatic interactions between the probe and sample. We show that this is due to incorporation of temporal information into the PSF—an issue that would be difficult to account for analytically/computationally, but that is solved relatively easily in experiment. Our results outline a practical and easily implemented approach toward getting quantitative information out of SKPM.

## II. MEASUREMENT PRINCIPAL

### A. Signal acquisition

Figure 1a depicts an SKPM probe positioned above a sample and the feedback system used to acquire an estimate for the spatially varying surface potential of interest,  $V_S \equiv V_S(x)$ . The probe vibrates vertically at a fixed amplitude and frequency, while a potential  $V$  is applied to the electrode at or below the sample. The current drawn to the probe due to the vibration is measured by an electrometer ( $E$ ) and further amplified by a lock-in amplifier which extracts the current signal due to the probe vibration and rejects noise at other frequencies. The signal acquired by SKPM is the value of the voltage,  $V$ , required to minimise the current induced in the probe as it is vibrated. This is accomplished by using feedback on the lock-in signal, *e.g.*, sending it to proportional-integral-differential (PID) electronics and adjusting  $V$  until the current amplitude is zero. In the naïve version of the analysis, the probe-sample system is assumed to form a capacitor, where the image charge drawn to the probe is given by

$$Q(t) = C(h(t))(V - V_S). \quad (1)$$

Here,  $C(h)$  is the capacitance, and  $h(t)$  is the time-varying height of the probe above the sample. By differentiating Eq. 1 with respect to time, setting equal to zero, and defining for  $V_m \equiv V$  in this condition, we find

$$0 = \frac{dQ}{dt} = \frac{dh}{dt} \frac{dC}{dh} (V_m - V_S). \quad (2)$$

Hence, for finite derivatives  $dh/dt$  and  $dC/dh$ , we see that this condition is satisfied when

$$V_m(x) = V_S(x). \quad (3)$$

In other words, the simplest interpretation of raw SKPM data is that it is an exact, point-by-point copy of the surface potential of interest.

The above analysis doesn't account for the finite size of the probe or long-range electrostatic interactions. These contributions can be incorporated by replacing the simple capacitance,  $C(h)$ , with an integral over a distributed capacitance,  $\mathcal{C}(h, x)$ <sup>12,13</sup>. In this case, the SKPM condition becomes

$$0 = \frac{d}{dh} \int_S (V_m(x) - V_S(\xi - x)) \mathcal{C}(h, \xi) d\xi, \quad (4)$$

where  $\xi$  is an integration variable. Solving this expression for  $V_m$  gives

$$V_m(x) = \int_S P(x, \xi) V_S(\xi) d\xi \quad (5)$$

where we define the PSF,  $P(x, \xi)$ , which accounts for the terms involving the interaction of the probe at location  $x$  with different sample positions  $\xi$ . Hence, a slightly more sophisticated analysis reveals that a raw SKPM measurement is the convolution of the underlying signal with a point spread function corresponding to the finite size of the probe and long-range interactions.

In practice, the situation is more complicated still, though for less obvious reasons. The measured signal depends not only on the electrostatic interactions between the probe and the sample, but also on the feedback system that measures the current and applies the voltage,  $V$ . Both the PID and lock-in amplifier require finite response times to produce stable signals. If the probe travels a significant distance over these timescales, then information from a range of locations is incorporated into the measurement. Additionally, faster scan speeds can introduce additional mechanical noise which will further distort the measured signal. Only for a stable system and when the probe is held at each location for long time relative to the response times of the PID/lock-in do we recover Eq. 5. Assuming these processes are linear, we can still write the measured voltage as a purely spatial convolution over a point spread function, but one that is velocity dependent; in other words,

$$V_m(x) = \int P(v|x, \xi) V_S(\xi) d\xi. \quad (6)$$

As the scan velocity approaches zero,  $P(v|x, \xi) \rightarrow P(x, \xi)$ , and the “fast scan” regime (Eq. 6) becomes equivalent to the “slow scan” regime (Eq. 5).

### B. Signal deconvolution

In the previous section, we discussed the forward problem: given an underlying surface potential,  $V_S(x)$ , determine the

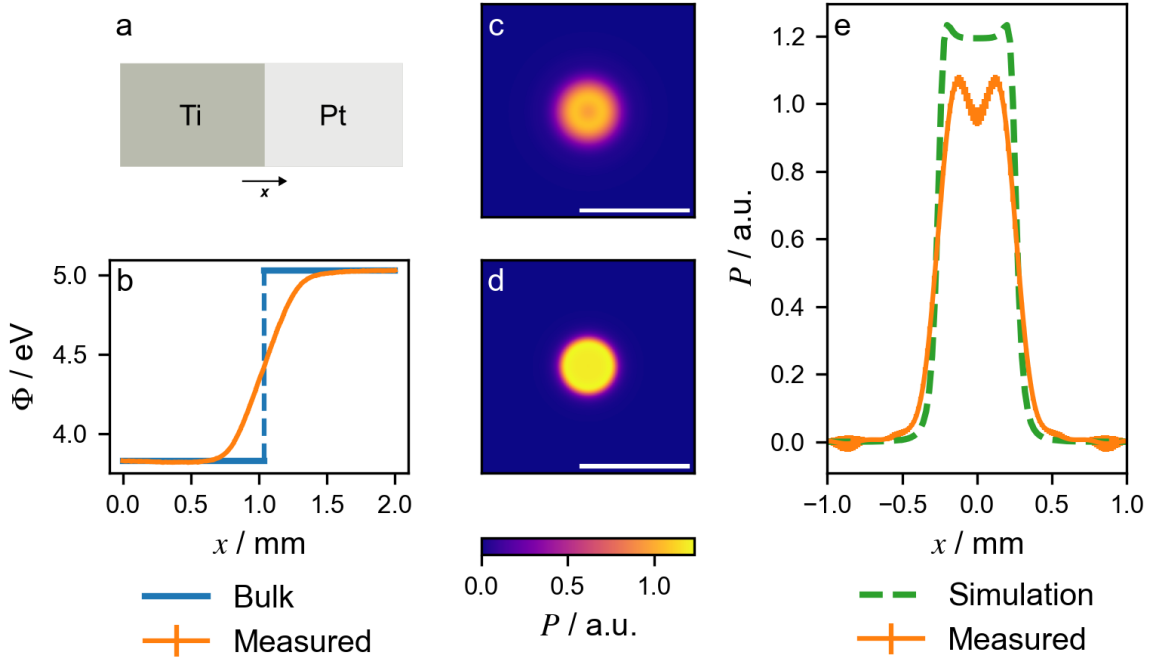


FIG. 2. **Comparison between a PSF estimated using an edge measurement and a simulated PSF.** **a** Scanning an edge created at the boundary between two metals with distinct work functions produces **b** an estimate for the system edge spread function (ESF) along the scan direction. **c** Shows the system PSF estimated from the ESF measurement by assuming that the probe is rotationally symmetric. **d,e** Simulations produce a PSF with a similar width and qualitatively similar shape, but show non-negligible differences due to variations between the simulation geometry and the real probe. All scale bars correspond to 1 mm.

resulting measurement,  $V_m(x)$ . However, what is usually required is the solution to the inverse problem: given the measurement,  $V_m(x)$ , determine the underlying signal,  $V_S(x)$  (*i.e.*, recover Fig. 1c from Fig. 1b). We start by writing the convolution over the PSF more compactly as

$$V_m = V_S \otimes P. \quad (7)$$

We would like to find an estimate for the true surface voltage map,  $\bar{V}_S$ . In the absence of measurement noise, and for a non-vanishing  $P$ , we can exactly recover the true surface voltage map,  $V_S$ , by

$$\bar{V}_S = V_m \otimes P^{-1} = (V_S \otimes P) \otimes P^{-1} = V_S, \quad (8)$$

where  $\otimes P^{-1}$  denotes the deconvolution with respect to  $P$ . This expression is relatively easy to calculate by taking advantage of the convolution theorem, *i.e.*

$$\bar{V}_S = \mathcal{F}^{-1} \left( \frac{\mathcal{F}(V_m)}{\mathcal{F}(P)} \right), \quad (9)$$

where  $\mathcal{F}$  and  $\mathcal{F}^{-1}$  represent the Fourier transform and inverse Fourier transform, respectively.

Real systems suffer from measurement noise, which renders the equivalence of  $\bar{V}_S$  and  $V_S$  in Eq. 8 unattainable in practice. Mathematically, independent sources of noise,  $N$ , enter into the equation as  $V_m = V_S \otimes P + N$ , and contain high-frequency components which deconvolution can amplify. To reduce the effect of this, one approach is to simply apply a

low-pass filter to  $V_m$ , which can be heuristically motivated given the finite size of probes<sup>18</sup>. However, in order to avoid discarding higher frequency information unnecessarily, an alternative is to use a weighted deconvolution, such as a Wiener filter<sup>12,13</sup>. Mathematically, this manifests itself as a modification to Eq. 9:

$$\bar{V}_S = \mathcal{F}^{-1} \left( \frac{\mathcal{F}(V_m)}{\mathcal{F}(P)} \cdot \left( \frac{|\mathcal{F}(P)|^2}{|\mathcal{F}(P)|^2 + \frac{1}{\text{SNR}(f)}} \right) \right), \quad (10)$$

where,  $\text{SNR}(f)$  is the signal to noise ratio as a function of spatial frequency. The SNR can either be measured (*e.g.*, by calculating the power spectral density of representative samples with known properties), or in certain circumstances assumed in conjunction with a frequency-relationship for the noise (*e.g.* Brownian noise  $1/f^2$ , pink noise  $1/f$ , *etc.*)

### III. TARGET FABRICATION & MEASUREMENT

To experimentally determine the PSFs, we fabricate calibration targets using metals with different work functions. We work with two different types: an edge target, which produces a large signal but only provides information about the PSF in one direction<sup>19,20</sup>; and a disc target, which allows convenient measurement of the full 2-dimensional PSF from a single 2-dimensional scan. We utilise the edge target for measuring the slow scan PSF (Eq. 5) where we assume rotational symmetry of the PSF and are interested in a very accurate low

noise estimate for the probe PSF. We use the disc target for estimating the fast scan PSF (Eq. 6) where the PSF is highly non-axisymmetric and our priority is on performing measurements in reasonable amounts of time under practical conditions.

We fabricate both targets using electron beam evaporation to deposit thin layers of different metals; full details are provided in the Supplemental Materials (SM). The edge target consists of a layer of platinum deposited on a titanium coated glass slide. The physical height of the platinum layer is small (12 nm) compared to the sample-tip separation (60  $\mu\text{m}$ ) so that its geometric influence can be ignored. These metals are chosen for their relatively large work function difference, which due to Fermi equalisation leads to a large contact potential difference and correspondingly large SKPM signal ( $\sim 1$  V). The disc target consists of a small, circular (400  $\mu\text{m}$  diameter) gold disc deposited on a silicon wafer, creating a contact potential difference on the order of 0.5 eV. As with the edge target, the height of the gold-titanium disc is small (103 nm) compared to the scan height.

We perform SKPM measurements using a commercially available device (Biologic, M470). When SKPM is used for work function measurements, the signal ( $\Delta\Phi$ ) is a relative measurement of the difference in work function between the probe and sample. As we explain in the SM, we convert relative work function differences to absolute work function values by first measuring the SKPM voltage using a reference sample of highly ordered pyrolytic graphite (HOPG). The work function is then given by  $\Phi = \Delta\Phi + \Delta\Phi_{\text{HOPG}}$ , where  $\Delta\Phi_{\text{HOPG}}$  is the difference between the literature value for the HOPG work function and the measured value. To estimate the SNR for deconvolution (*i.e.*, Eq. 10), we look at the power spectral density of a relatively flat region and use this to estimate a power-law relationship between SNR and frequency.

To demonstrate the effect of acquisition parameters and the temporal dependence of acquired measurements, we perform slow scans with step-mode acquisition and fast scans with sweep-mode acquisition. The step-mode acquisition entails moving the probe between specific points and holding it fixed until the SKPM signal has stabilised (*i.e.*, until we can ignore effects from the movement and settling time of the PID/lock-in amplifier). Sweep-mode acquisition involves moving the probe continuously across the sample at a constant velocity, resulting in a temporally distorted signal depending on the scan speed and feedback parameters.

## IV. RESULTS & DISCUSSION

### A. Experimentally determining PSFs in the quasi-static limit

We now demonstrate how a PSF can be determined experimentally. We start in the slow scan regime, *i.e.* at speeds that are small enough such that Eq. 5 applies. The main difficulty in measuring the slow scan PSF is signal strength compared to measurement noise. Signal strength can be improved by increasing the work function difference between the target and surface or increasing the size of the target, while noise can be

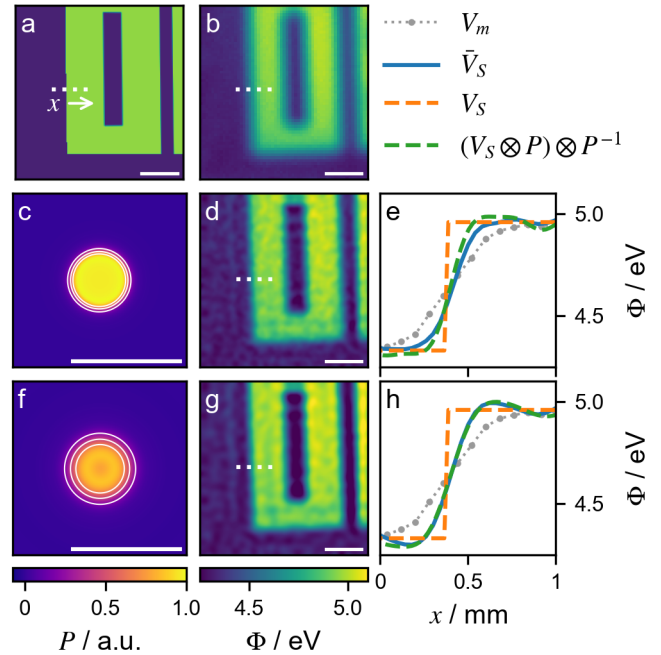


**FIG. 3. Comparison between deconvolution with different PSFs in slow scans.** **a** Scanning a gold-on-silicon target ( $V_S$ ) with sharp features produces **b** a measured ( $V_m$ ) signal with low contrast and blurred-out features. **c–e** Deconvolution with **c** the simulated PSF from Fig. 2**d** produces **d** an image with higher contrast; however, as shown in **e**, a slice through the deconvolved image ( $\bar{V}_S$ ) differs from the ideal scenario ( $(V_S \otimes P) \otimes P^{-1}$ ). **f–h** The experimentally measured probe PSF produces a improved estimate for the original signal. Scale bars show 1 mm.

reduced with repeated measurements and reduced scan speed. We have found that a good solution for the slow-scan regime is to perform a 1-dimensional scan over a sharp edge between two materials with distinct work functions (Figure 2**a**). Even so, extremely slow speeds are required for probe motion to be completely negligible. We utilize a step size of 5  $\mu\text{m}$ , moving at 5  $\mu\text{m}/\text{s}$  between points and dwelling at each point for 3.5 s. To improve SNR, we repeat and average multiple lines. In this process, a *single* line scan takes approximately 45 minutes, and the ensemble takes more than seven hours. The final result is shown in Fig. 2**b**.

To obtain the PSF, we first calculate the line spread function from the derivative of the line scan, and then in Fourier space we interpolate the 1-dimensional transform of the line spread function to a 2-dimensional map assuming rotational symmetry. Taking the inverse transform we get an approximation of the real space PSF (see SM for full details). The result is shown in (Fig. 2**c**). The cross section of this PSF (Fig. 2**e**) has a non-intuitive feature: a ring of higher intensity towards the edge of the probe. To investigate this further and perform a sanity-check of our strategy, we perform numerical simulations for a second, independent estimate of the PSF (Fig. 2**d,e**; see SM for details on simulations). The simulations produce a decent estimate for the PSF, but the differences are non-negligible. The simulated PSF has a higher amplitude, is slightly narrower, and exhibits a more subdued ring

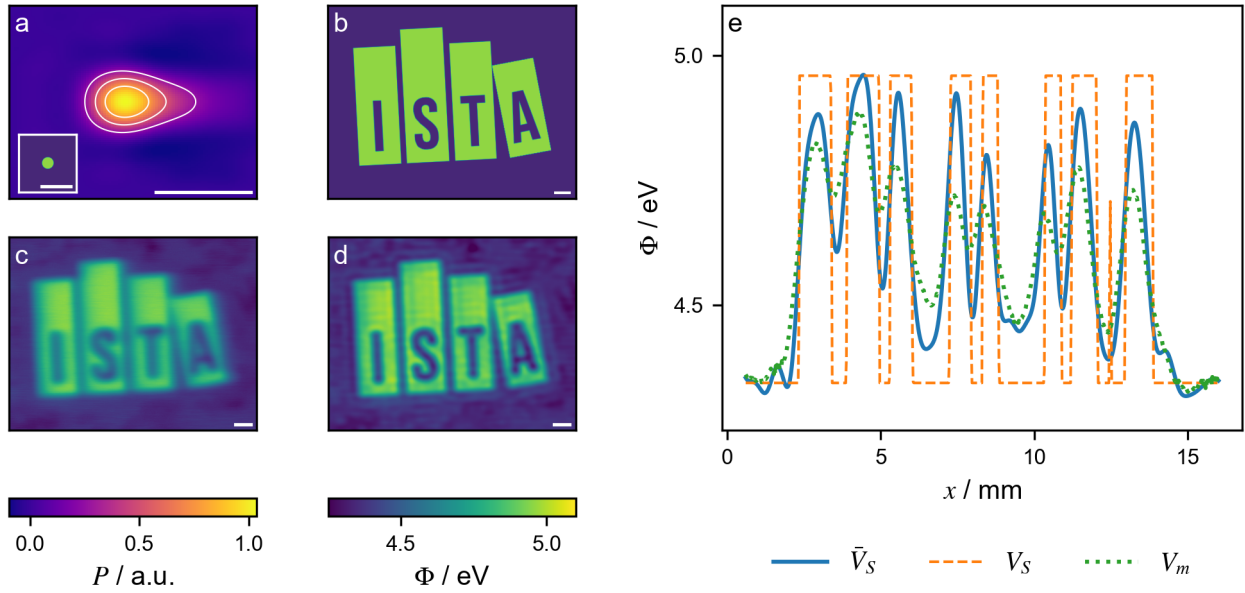


FIG. 4. **PSF and deconvolution for a fast scan.** **a** Fast scans produce a significantly broadened and asymmetric PSF ( $P$ ), particularly along the scan direction. **b,c** When the same parameters are used to scan a large target ( $V_S$ , **b**), this produces a blurred-out image ( $V_m$ , **c**). **d** Deconvolution of the measured signal with the PSF produces a significantly improved estimate for the underlying signal ( $\bar{V}_S$ ). **e** A slice shows quantitatively how the contrast is improved by the deconvolution. Scale bars correspond to 1 mm.

at the edge. We suspect these differences are due to physical features of the probe that the idealised simulation geometry cannot capture. For example, visual inspection of the probe reveals it is not perfectly cylindrical, and high-speed video reveals subtle horizontal vibrations in addition to the vertical motion (see SM). This speculation is supported qualitatively by the fact that in our simulations, we observe that even small changes to the probe shape (*e.g.* rounding edges) can have a significant effect on the PSF (see SM). The inability of simulations to faithfully reproduce the experiments even in the slow-scan regime highlight the need for measuring PSFs.

With a PSF in hand, we turn our attention to reconstructing an underlying signal source from an actual measurement. Fig. 3a illustrates our gold-on-silicon target, where the pattern consists a series of vertical/horizontal stripes switching between the two materials. We scan over this target at a slightly lower resolution (80  $\mu\text{m}$  steps) and slightly larger speed (20  $\mu\text{m}/\text{s}$  with 0.6 s dwell time) so that the scan doesn't take unreasonably long. This produces the measured voltage map,  $V_m$ , of Fig. 3b. Using Eq. 10 and the simulated and measured probe PSFs of Fig. 2, we find that we can indeed recover estimates with improved resolution/contrast (Fig. 3c–h). We show in the SM that these recoveries already suffer from slightly elevated scan speed; trying to eliminate temporal information in the PSF entails compromises between speed and resolution that are difficult to balance. As we show in the next section, the better solution is to simply incorporate the probe motion into the PSF.

## B. Determining PSFs for rapid measurements

Without compromising scan speed, we would like to be able to characterise large patterns of interest with high spatial resolution. As mentioned previously, when the distortions introduced by fast scanning are linear, then one can anticipate a velocity-dependent PSF,  $P(v|x, \xi)$ , that nonetheless connects the measured signal,  $V_m$ , to the underlying signal,  $V_S$ , via spatial convolution, as in Eq. 6. In order to acquire this PSF, we straightforwardly perform a scan with the same measurement parameters as we use for the sample measurement. While we could repeat the procedure involving the edge PSF described above, we now no longer have to worry about scanning slowly to stay in a regime where Eq. 5 is applicable. Moreover, scanning fast creates an additional source of broadening to the PSF, making the use of larger targets more practical. Figure 4 shows how we put this into practice. To get a velocity-dependent scan, we now operate the SKPM in sweep (continuous) mode (as opposed to step mode), and with a significantly higher speed of 200  $\mu\text{m}/\text{s}$ . The size of the disk renders a large PSF signal, helping to ameliorate the noise issues mentioned previously. As is visually apparent in the image of the PSF itself (Fig. 4a), the velocity dependence blurs the image in the scan direction (left to right).

Next, we scan a large and detailed target ( $\sim 1.5 \times 1.0 \text{ cm}^2$ ), as shown in Fig. 4b, which again consists of gold patterned onto a silicon wafer. The scan parameters are intentionally set to be the same as in the PSF of Fig. 4a. The resulting raw voltage map is shown in Fig. 4c. Comparing this to the slower scans of Fig. 2, the spatial blurring is much more apparent. Moreover, it is evident that this has the same left-to-right tail

as the corresponding PSF. However, upon spatially deconvolving this scan with the corresponding PSF, the blur is reduced (Fig. 4d). We validate this quantitatively in Fig. 4e, where we plot the target, raw, and recovered values on top of each other, illustrating that the recovered voltages are much sharper and lie much closer to the target values.

## V. CONCLUSION

In this work we demonstrate how the PSFs relevant to scanning Kelvin probe microscopy (SKPM) can be experimentally determined. We find that measured PSFs can differ significantly from those estimated using simulations, especially for rapid scans where the finite response of the feedback system and additional noise further broaden the PSFs. We demonstrate that a practical approach for accounting for the effect of noise in a scan is to measure the PSF using similar scan parameters to those used during measurement acquisition. We utilize two methods for estimating PSFs: one using a edge target, which provides good signal strength but only gives information about the PSF in one direction; and the second using a disc, which provides information about the full 2-dimensional PSF from a single 2-dimensional scan. While both methods could be used to acquire PSFs, we found that the disc was particularly useful for faster scans, where the PSFs tend to be non-axisymmetric. The edge method is more suited to acquiring lower noise PSFs but requires assumptions about the PSF symmetry or multiple measurements with different edge angles to estimate the 2-dimensional PSF.

While the larger probes used in SKPM allow direct measurement of the PSF, for smaller probes the required spot size and the corresponding decrease in the signal to noise ratio makes experimental measurement of such PSFs difficult. We explore targets involving work function differences between metals, however other approaches such as depositing charge spots or creating a artificial potential step<sup>21</sup> could further improve the signal to noise ratio. Although we focused on SKPM, this procedure could also be useful for characterising and correcting for temporal effects in related methods<sup>15</sup>. Additional modelling of the signal acquisition pipeline could also be useful for determining the effective measurement PSFs from simulated PSFs, this could be particularly relevant for smaller probes such as the nano-scale probes used in KPFM. The results presented here could be useful for scanning larger samples, particularly with larger probes at faster scanning speeds while achieving decent resolution in the reconstructed images.

## ACKNOWLEDGEMENTS

This project has received funding from the European Research Council (ERC) under the European Union’s Horizon 2020 research and innovation program (Grant agreement No. 949120). This research was supported by the Scientific Service Units of The Institute of Science and Technology Austria (ISTA) through resources provided by the Miba Machine

Shop, Nanofabrication Facility, Scientific Computing Facility, and Lab Support Facility. The authors wish to thank Dmytro Rak and Juan Carlos Sobarzo for letting us use their equipment. The authors wish to thank the contributions of the whole Waitukaitis group for useful discussions and feedback.

## AUTHOR DECLARATIONS

### Conflict of Interest

The authors have no conflicts to disclose.

### CRediT Author Statement

IL: Conceptualization; Formal analysis; Simulation; Investigation; Writing – Original Draft. FP: Investigation; Resources. LS: Resources. SW: Writing – Review & Editing; Supervision; Funding acquisition.

## DATA AVAILABILITY STATEMENT

The data that support the findings of this study are available from the corresponding author upon reasonable request.

## REFERENCES

- W. A. Zisman, “A new method of measuring contact potential differences in metals,” *Rev. Sci. Instrum.* **3**, 367–370 (1932).
- P. P. Craig and V. Radeka, “Stress Dependence of Contact Potential: The ac Kelvin Method,” *Rev. Sci. Instrum.* **41**, 258–264 (1970).
- A. Nazarov and D. Thierry, “Application of Scanning Kelvin Probe in the Study of Protective Paints,” *Front. Mater.* **6**, 462587 (2019).
- A. Nazarov, M.-G. Olivier, and D. Thierry, “SKP and FT-IR microscopy study of the paint corrosion de-adhesion from the surface of galvanized steel,” *Progress in Organic Coatings* **74**, 356–364 (2012), application of Electrochemical Techniques to Organic Coatings.
- H. T. Baytekin, A. Z. Patashinski, M. Branicki, B. Baytekin, S. Soh, and B. A. Grzybowski, “The Mosaic of Surface Charge in Contact Electrification,” *Science* **333**, 308–312 (2011).
- X. Bai, A. Riet, S. Xu, D. J. Lacks, and H. Wang, “Experimental and Simulation Investigation of the Nanoscale Charge Diffusion Process on a Dielectric Surface: Effects of Relative Humidity,” *J. Phys. Chem. C* **125**, 11677–11686 (2021).
- T. Hackl, G. Schitter, and P. Mesquida, “AC Kelvin Probe Force Microscopy Enables Charge Mapping in Water,” *ACS Nano* **16**, 17982–17990 (2022).
- Ørjan G. Martinsen and A. Heiskanen, “Chapter 7 - electrodes,” in *Bioimpedance and Bioelectricity Basics (Fourth Edition)*, edited by Ørjan G. Martinsen and A. Heiskanen (Academic Press, Oxford, 2023) fourth edition ed., pp. 175–248.
- M. Nonnenmacher, M. P. O’Boyle, and H. K. Wickramasinghe, “Kelvin probe force microscopy,” *Appl. Phys. Lett.* **58**, 2921–2923 (1991).
- T. Glatzel, U. Gysin, and E. Meyer, “Kelvin probe force microscopy for material characterization,” *Microscopy* **71**, i165–i173 (2022).
- W. Melitz, J. Shen, A. C. Kummel, and S. Lee, “Kelvin probe force microscopy and its application,” *Surf. Sci. Rep.* **66**, 1–27 (2011).
- G. Cohen, E. Halpern, S. U. Nanayakkara, J. M. Luther, C. Held, R. Bennewitz, A. Boag, and Y. Rosenwaks, “Reconstruction of surface potential

from Kelvin probe force microscopy images," *Nanotechnology* **24**, 295702 (2013).

<sup>13</sup>T. Machleidt, E. Sparrer, D. Kapusi, and K.-H. Franke, "Deconvolution of Kelvin probe force microscopy measurements—methodology and application," *Meas. Sci. Technol.* **20**, 084017 (2009).

<sup>14</sup>B. Ren, L. Chen, R. Chen, R. Ji, and Y. Wang, "Noise Reduction of Atomic Force Microscopy Measurement Data for Fitting Verification of Chemical Mechanical Planarization Model," *Electronics* **12**, 2422 (2023).

<sup>15</sup>M. Checa, A. S. Fuhr, C. Sun, R. Vasudevan, M. Ziatdinov, I. Ivanov, S. J. Yun, K. Xiao, A. Sehirlioglu, Y. Kim, P. Sharma, K. P. Kelley, N. Domingo, S. Jesse, and L. Collins, "High-speed mapping of surface charge dynamics using sparse scanning Kelvin probe force microscopy," *Nat. Commun.* **14**, 1–12 (2023).

<sup>16</sup>D. Ziegler, T. R. Meyer, R. Farnham, C. Brune, A. L. Bertozzi, and P. D. Ashby, "Improved accuracy and speed in scanning probe microscopy by image reconstruction from non-gridded position sensor data," *Nanotechnology* **24**, 335703 (2013).

<sup>17</sup>R. W. Cole, T. Jinadasa, and C. M. Brown, "Measuring and interpreting point spread functions to determine confocal microscope resolution and ensure quality control," *Nat. Protoc.* **6**, 1929–1941 (2011).

<sup>18</sup>F. Pertl, J. C. Sobarzo, L. Shafeek, T. Cramer, and S. Waitukaitis, "Quantifying nanoscale charge density features of contact-charged surfaces with an FEM/KPFM-hybrid approach," *Phys. Rev. Mater.* **6**, 125605 (2022).

<sup>19</sup>C. D. Claxton and R. C. Staunton, "Measurement of the point-spread function of a noisy imaging system," *J. Opt. Soc. Am. A, JOSAA* **25**, 159–170 (2008).

<sup>20</sup>X. Zhang, T. Kashti, D. Kella, T. Frank, D. Shaked, R. Ulichney, M. Fischer, and J. P. Allebach, "Measuring the modulation transfer function of image capture devices: what do the numbers really mean?" in *Proceedings Volume 8293, Image Quality and System Performance IX*, Vol. 8293 (SPIE, 2012) pp. 64–74.

<sup>21</sup>M. Brouillard, N. Bercu, U. Zschieschang, O. Simonetti, R. Mittapalli, H. Klauk, and L. Giraudet, "Experimental determination of the lateral resolution of surface electric potential measurements by Kelvin probe force microscopy using biased electrodes separated by a nanoscale gap and application to thin-film transistors," *Nanoscale Adv.* **4**, 2018–2028 (2022).

<sup>22</sup>U. Zerweck, C. Loppacher, T. Otto, S. Grafström, and L. M. Eng, "Accuracy and resolution limits of Kelvin probe force microscopy," *Phys. Rev. B* **71**, 125424 (2005).

<sup>23</sup>Th. Glatzel, M. Ch. Lux-Steiner, E. Strassburg, A. Boag, and Y. Rosenwaks, "Principles of Kelvin Probe Force Microscopy," in *Scanning Probe Microscopy* (Springer, New York, NY, New York, NY, USA, 2007) pp. 113–131.

<sup>24</sup>M. Salerno and S. Dante, "Scanning Kelvin Probe Microscopy: Challenges and Perspectives towards Increased Application on Biomaterials and Biological Samples," *Materials* **11** (2018), 10.3390/ma11060951.

<sup>25</sup>D. Hoffman and D. Leibowitz, "Effect of Substrate Potential on Al<sub>2</sub>O<sub>3</sub> Films Prepared by Electron Beam Evaporation," *J. Vac. Sci. Technol.* **9**, 326–329 (1972).

<sup>26</sup>F. Volmer, I. Seidler, T. Bisswanger, J.-S. Tu, L. R. Schreiber, C. Stampfer, and B. Beschoten, "How to solve problems in micro- and nanofabrication caused by the emission of electrons and charged metal atoms during e-beam evaporation," *J. Phys. D: Appl. Phys.* **54**, 225304 (2021).

<sup>27</sup>N. Turetta, F. Sedona, A. Liscio, M. Sambi, and P. Samori, "Au(111) Surface Contamination in Ambient Conditions: Unravelling the Dynamics of the Work Function in Air," *Adv. Mater. Interfaces* **8**, 2100068 (2021).

<sup>28</sup>Y. Yu, D. Lee, and B. Jeong, "The dependence of the work function of Pt(111) on surface carbon investigated with near ambient pressure X-ray photoelectron spectroscopy," *Appl. Surf. Sci.* **607**, 155005 (2023).

<sup>29</sup>R. Bai, N. L. Tolman, Z. Peng, and H. Liu, "Influence of Atmospheric Contaminants on the Work Function of Graphite," *Langmuir* **39**, 12159–12165 (2023).

<sup>30</sup>H. Sugimura, Y. Ishida, K. Hayashi, O. Takai, and N. Nakagiri, "Potential shielding by the surface water layer in Kelvin probe force microscopy," *Appl. Phys. Lett.* **80**, 1459–1461 (2002).

# Beyond the blur: using experimental point spread functions to help scanning Kelvin probe microscopy reach its full potential

## (Supplementary Material)

Isaac C.D. Lenton, Felix Pertl, Lubuna Shafeek, Scott R. Waitukaitis

April 2024

## S1 Experimental Methods

### S1.1 SKPM measurement

For all SKPM measurements we used the Biologic M470 scanning kelvin probe module. Except where otherwise noted, all measurements used a  $500\ \mu\text{m}$  diameter probe (U-SKP370/1, Biologic). The sample was mounted on a tip-tilt-rotation stage (TTR001/M, Thorlabs) with a custom sample holder. For most samples, we used 100 mm diameter silicon wafers as these were easy to handle and mount on the stage. The wafers were electrically connected to the SKPM by attaching a piece of copper tape (AT526, Advance Tapes) near the edge of the wafer to more easily allow connecting the M470. To ensure a good electrical connection between the tape and wafer, we scratched the wafer surface with a diamond scribe and used silver paint (123-9911, RS Pro) to electrically connect the scratched region to the tape. We connected the platinum-titanium target using a similar method except the silver paint could be applied directly to the platinum without needing to first scratch the surface. Prior to measurement, samples were levelled by making multiple capacitive height measurements at different locations across the sample and adjusting the stage. The probe was then positioned at the desired height above the sample ( $60\ \mu\text{m}$  from the surface, except where otherwise noted). Key scan parameters are given in Table S1.

	Pt-Ti Edge	Course Scan	Fast Scan	Line Scans
Pixel Size ( $\mu\text{m}$ )	5	$80 \times 80$	$20 \times 40$	20
Movement Speed ( $\mu\text{m/s}$ )	5	20	200	20
Scan Mode	Step	Step	Sweep	Step
Acquisition rate (S/s)	8000	8000	—	8000
Acquisition duration (S)	20000	4000	—	12000
Pre-delay (s)	1	0.1	—	0.1

Table S1: Scan parameters used throughout this work for: platinum-titanium (Pt-Ti) Edge (Fig. 2), Course Scan (Fig. 3), Fast Scan (Figure 4), and Line Scans (Figure S4). For step-mode scans, the dwell time is estimated from acquisition duration and pre-delay time.

### S1.2 Work function calibration

We calibrated the SKPM signal by measuring the potential using freshly exfoliated Highly Ordered Pyrolytic Graphite (HOPG, G3389, Agar Scientific). HOPG was freshly exfoliated using tape (Scotch Magic Tape, Scotch Brand). Care was taken to completely remove a whole layer of graphite. After mounting and levelling the sample, the SKPM probe was positioned  $100\ \mu\text{m}$  from the HOPG surface and the potential was measured for different system gain parameters. Different SKPM probes can have different calibration factors. Table S2 compares 2 large probes (U-SKP370/1, Biologic) and 1 small (U-SKP-150). We noticed that the voltage

offset depends not only on the probe, but also the electrometer gain. The relationship between offset and gain does not appear to be independent of probe, possibly due to the shift in phase required to maximise the signal. To convert the relative SKPM signal to an absolute work function difference, we compare the measured value for HOPG with the literature value of HOPG to give us an estimate for the work function offset  $\Delta\Phi_{\text{HOPG}}$ . The results presented in this work all used Probe 3.

	Probe 1	Probe 2	Probe 3
Diameter ( $\mu\text{m}$ )	500	150	500
LIA Phase (deg)	136	131	133
Voltage (V)			
Gain: 1	0.016	-0.183	0.006
Gain: 10	0.022	-0.167	0.124
Gain: 100	0.0140	-0.17	0.065
Gain: 1000	2.67	4.4	2.5
Gain: 10000	0.723	2.2	0.52

Table S2: Measured SKPM voltages against HOPG calibration target for different tip and gain parameters.

### S1.3 Platinum-titanium sample fabrication

To measure the point spread function from an edge (Fig. ??), we created a calibration target with platinum and titanium, since these materials have a large work function difference. A glass slide was cleaned using Acetone (2 minutes ultrasonic bath) and rinsed with isopropanol before baking at 140°C for 2 minutes to remove any residual water. The glass was then cleaned using a plasma cleaner (1 minutes, 0.5 mbar O<sub>2</sub>, 240 W), and immediately transferred to the electron beam evaporator (HV Plassy, Plassys Bestek) and pumped to  $5 \times 10^{-7}$  mBar. 3 nm titanium was evaporated at 0.1 nm/s. The chamber was vented and a mask was applied to half of the titanium surface (Kepton tape). The system was pumped again to  $5 \times 10^{-7}$  mBar, 2 nm additional titanium was deposited at 0.1 nm/s and 10 nm Pt at 0.1 nm/s. Measurements using this sample were performed throughout the following week. We noted that the work function values changed significantly over the following months when this sample was reused, we suspect this is due to surface contamination or another deterioration process.

### S1.4 PSF estimation from edge

To estimate the quasi-static PSF, we first calculated the line spread function from the measured edge spread function. In order to reduce the noise, we averaged multiple scans of the edge and low-pass filtered the result. The mean of each scan was subtracted to account for instrument drift between scans and the uncertainty was estimated from the standard deviation between scans after subtracting the mean. The numerical derivative was then calculated using a 4-point central difference method and the result low-pass filtered to further reduce noise. Errors were propagated through the low-pass and numerical difference steps assuming the measurement uncertainty is significantly larger than the additional uncertainty introduced from the numerical differentiation. To estimate the PSF from the line spread function, we calculated the Fourier transform of the line spread function and interpolated the 1-D Fourier transform radially into 2-D before taking the inverse Fourier transform to give the point spread function. Errors were propagated using the same interpolation approach, however, we note that this may underestimate the errors in the final PSF.

### S1.5 Gold lift-off lithography sample fabrication

To fabricate the gold-on-silicon samples (used in Fig. ?? & Fig. ??) we used a photolithography procedure, briefly outlined below. New silicon wafers (p-type, Boron,  $\langle 100 \rangle$ , polished) were cleaned in isopropanol for 2 minutes in an ultrasonic bath on high power and then rinsed briefly with additional isopropanol. Wafers were dried using nitrogen, and heated on a hot plate at 170°C for 2 minutes. An adhesion promoter (VM652 – a solution of a-amino propyltriethoxysilane in an organic solvent) was spin coated on the wafer to assist in adhesion of the lift-off resist. A layer of LOR5B (Micro resist technology) resist was spin coated on the wafer

(2000 rpm for 45 s). The wafers were baked on a hotplate for 5 minutes at 170°C. Two layers of positive photoresist (Microposit S1818, Micro resist technology) were then spin coated on top of the lift-off resist (6,000 rpm for 30 s). After each photoresist coating, the wafer was baked for 1 minute at 115°C.

The coated wafers were then UV exposed using a mask aligner (EVG 610, EV Group) with a mercury bulb light source. Patterns for the calibration targets and work function targets were designed using Creo Parametric and printed on 0.18mm Polyethylene terephthalate (PET) film (JD PhotoData). The mask was mounted on a 1.5 mm glass plate to more easily load it into the mask aligner. The wafer and pattern was then loaded into the mask aligner and exposed to 150mJ/cm<sup>2</sup>. Post exposure, the wafer was baked for 1 minute at 115°C.

The pattern was then developed by immersion in a beaker of MF-319 Developer (Micro resist technology) for 40 seconds and then transferred to a beaker with de-ionised water and visually inspected. If the sample needed additional development, the sample was transferred back into the MF-319 beaker for 5 second intervals. The sample was then rinsed in two baths of de-ionised water and dried with nitrogen.

For metal deposition we used an electron beam evaporator (HV Plassy, Plassys Bestek). We first prepared the wafer surface using oxygen plasma cleaning (240 W, 25 sccm O<sub>2</sub>, 1 minute). Immediately following, we transferred the wafer to the evaporator and pumped down to bellow 10<sup>-6</sup> mBar. To improve adhesion of the gold, we first deposited 3 nm titanium (0.4 nm/s) before depositing 100nm gold (0.6 nm/s). The increased thickness compared to the titanium-platinum target was chosen to improve durability during handling and future reuse of these targets.

For the lift-off step, we heated DMSO (MicroChemicals) to 50°C in an ultrasonic bath. The wafer was placed in the DMSO bath for 6 minutes and ultrasonic on low power until lift-off was complete. Finally the wafer was rinsed in isopropanol and dried with nitrogen.

## S1.6 Low cost silver calibration target

As an alternative to using targets fabricated using lithography, we also briefly explored using conductive silver paint as a lower cost alternative. To make the low cost target we used a metal wire (diameter 800  $\mu\text{m}$ ) dipped in conductive silver paint (123-9911, RS Pro). By carefully contacting the end of the wire with the wafer, we were able to create spots between about 200-400  $\mu\text{m}$  (often multiple attempts were required to produce a nice spot).

## S1.7 PSF estimation from disc scans

To estimate the PSF for fast scans, we used a 400  $\mu\text{m}$  diameter gold-on-silicon discs created using the gold lift-off procedure described above. The measured PSFs have a lot of high frequency noise which can adversely affect the deconvolution. To reduce the noise, we filter the measured PSF. A brief summary of the filtering procedure is outlined bellow.

1. *Load data from SKPM output file.*
2. *De-trend data.* While we attempted to level each sample before scanning, there is often a small tilt still remaining. We attempt to remove this tilt by de-trending the data based on the average slope of the edge values.
3. *Calculate fast Fourier transform.* We apply most of the filtering in frequency space. Before calculating the Fourier transform we pad the measurement with zeros to avoid introducing edge artefacts.
4. *Low pass filter.* To remove the bulk of the high frequency noise, we apply a low pass filter. The choice of cut-off frequency was chosen empirically based on the target signal strength, probe diameter, and inspection of the frequency spectrum image.
5. *Target normalisation.* The ideal calibration target should be much smaller than the probe diameter; however, smaller targets result in poorer signal-to-noise ratios. When using larger calibration targets, we get better signal-to-noise ratios but we need to account for the distortion to the PSF shape. To do this, we divide by the expected frequency spectrum of our calibration target (for circular targets, this

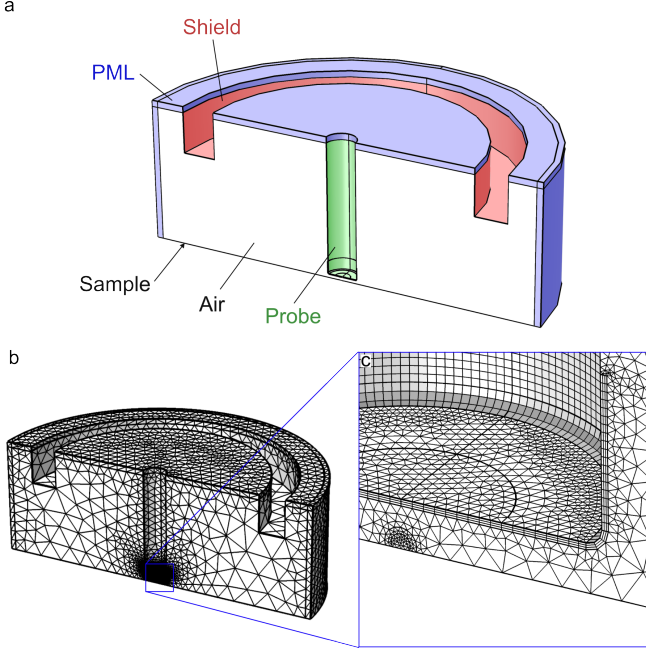


Figure S1: **a** The COMSOL model and **b,c** mesh used for PSF simulations. The model shows the different regions used in the COMSOL simulation including the perfectly matched boundary layer (PML), the conductive layers for the Shield, Probe and Sample, and the air volume being simulated.

is a Jinc function). For calibration targets much smaller than the probe diameter, the frequency space normalisation has little affect since most of the information in frequency space is contained within the central lobe of the Jinc.

6. *Inverse Fourier transform.* We then calculate the inverse fourier transform to give the filtered PSF. We pad the frequency space image in order to smoothly upsample our PSF (this is important for low-resolution PSFs).
7. *Centring, normalisation and interpolation.* To make it easier to work with our PSF in other routines, we normalise the PSF so the maximum value is 1 (discarding sign), centre the PSF, and create a regular grid interpolator for our PSF. This makes it easier to apply our pre-calculated PSFs to new datasets, regardless of the pixel aspect ratio or resolution.

## S2 COMSOL simulations

To explore the effect of tip geometry on the probe PSF, we built a COMSOL (5.3a) model, shown in Figure S1. The model is mirror symmetric and includes the sample surface, a portion of the probe and shield, and a surrounding perfectly matched layer (PML). Additional mesh refinement was included around the point defect and around the tip of the probe. The mesh size was chosen in order to produce a smooth surface charge density on the surface and probe. Model parameters are given in Table S3.

To calculate the PSF using this model, we calculated the surface charge on the probe for two different situations: when 1 V was applied to the entire sample; and when 0 V is applied to the sample except for a small disc with non-zero voltage. The probe is positioned at  $a = \pm 15 \mu\text{m}$  from its equilibrium position above the sample. The dimensionless PSF signal is estimated with

$$\text{PSF} \propto \frac{Q(a_+, x) - Q(a_-, x)}{Q(a_+) - Q(a_-)} \quad (1)$$

where  $Q(a_{\pm}, x)$  denotes the surface charge on the tip measured with the disc at position  $x$ , and  $Q(a_{\pm})$  is for

Parameter	Value	Parameter	Value
Tip radius	0.25 mm	Shield outer radius	2.79 mm
PML thickness	0.1 mm	Shield inner radius	2.24 mm
Tip height	60 $\mu\text{m}$	Tip displacement	$\pm 15 \mu\text{m}$
Tip rounding	20 $\mu\text{m}$	Target radius	12 $\mu\text{m}$
Far-field radius	3.35 mm	Shield height	1.56 mm
Far-field height	2.34 mm		

Table S3: Key parameters used in COMSOL simulation.

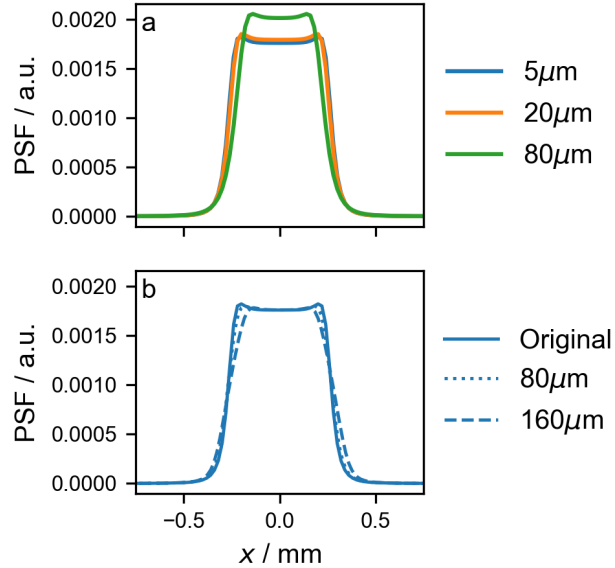


Figure S2: **a** Simulated PSFs with different tip rounding. **b** Low-pass filtered PSFs calculated by convolving a circular aperture with diameters 80  $\mu\text{m}$  and 160  $\mu\text{m}$  with the 5  $\mu\text{m}$  simulated PSF.

a uniform sample potential.

Rounding of the tip has an effect on the PSF shape. Figure S2a compares tips of the same diameter but with different radius of curvature around the bottom edge of the cylindrical shape. Higher radius of curvature produces a more narrow PSF, but all PSFs still have the same flattop shape with peaks near the edge. To explore the effect of a band-limited measurement of the PSF (such as for too coarse resolution or too high scan speeds), we also looked at low-pass filtering the 5  $\mu\text{m}$  PSF (Figure ??b). The low-pass filter removes the edge features. This is not the behaviour we see in the experimentally measured PSF in Figure ??e. Instead, this leads us to believe that the difference between the simulated and measured PSFs is related to our model for the tip geometry (the physical probe is not as uniform and visible scratches can be seen in the tip, possibly caused by use or manufacturing defects).

### S3 Fast edge scan PSF estimation

The edge target can also be used for PSF estimation for fast scans as long as the scan is not so fast that the PSF becomes significantly asymmetric. Figure S3 demonstrates how the PSF shape changes when the scan speed is increased from 5  $\mu\text{m/s}$  to 100  $\mu\text{m/s}$ . This scan speed still produces a very symmetric PSF, however the PSF is significantly broadened (equivalent to applying a 800  $\mu\text{m}$  low-pass filter). The broadening means that the effective resolution is much lower, and using a larger calibration target for these higher speed scans (such as a 400  $\mu\text{m}$  gold disc) should not significantly affect the estimate for the PSF. While there may still be some effect from using a 400  $\mu\text{m}$  disc as a calibration target, our pre-processing step for fitting the PSF

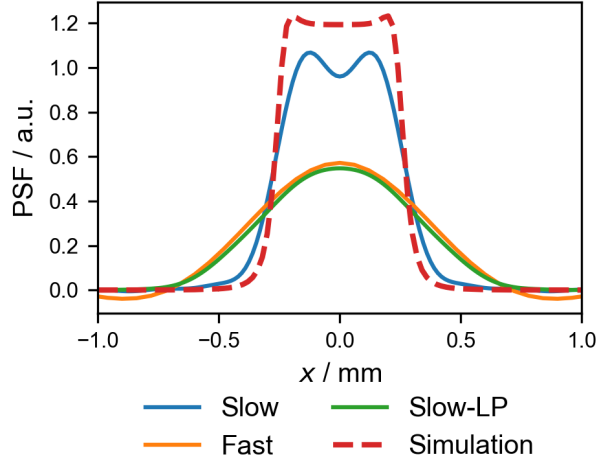


Figure S3: PSFs constructed from an edge scan using a slow ( $5\mu\text{m/s}$ ) and fast ( $100\mu\text{m/s}$ ) scan speeds. The simulation and slow scan correspond to the results presented in Figure ???. Slow-LP shows the fast scan with a  $800\mu\text{m}$  low pass filter.

and deconvolving by the disc diameter should reduce the effect in the overall measurement.

## S4 Disc target size

To explore the effect of disc target size on PSF estimation, we also measured different disc with different diameters. The scans are shown in Figure S4. A slightly slower scan speed was used for these scans (helping to resolve the smaller target). All three targets produced a similar shape, although there is still a tiny effect of the target diameter. As expected, the scan of the smaller disc is significantly more noisy. These estiamtes are all much smaller than the slow mesurement PSF shown in Figure S3, suggesting that all the targets are small enough for the fast scan speeds used in Figure ??.

Figure S4 also shows a line scan of a silver calibration target. Although this target is visibly not as circular or uniform as the gold targets, these defects are small compared to the effective measurement PSF, and the results are comparable to the gold targets.

## S5 PSF measurement resolution

Figure S5 compares scan resolution and the estimated PSF shape. While there are some variations between resolution and additional error introduced between the lower resolution scan, the filtering applied for estimating the PSF from these scans seems to produce reasonable/repeatable results.

## S6 Measurement of tip vibration

Using a fast camera (1200 frames per second), we recorded the motion of the SKPM tip. Stills and the estimated trajectory are shown in Figure S6. The tip is vibrated at 80 Hz, and we can clearly see the axial motion of the tip on the camera. We also observe a fair amount or lateral motion, which will likely lead to an effective larger diameter tip. This video was recorded with the probe set to track a fixed position. We expect that the lateral vibrations would increase when the tip is in motion.

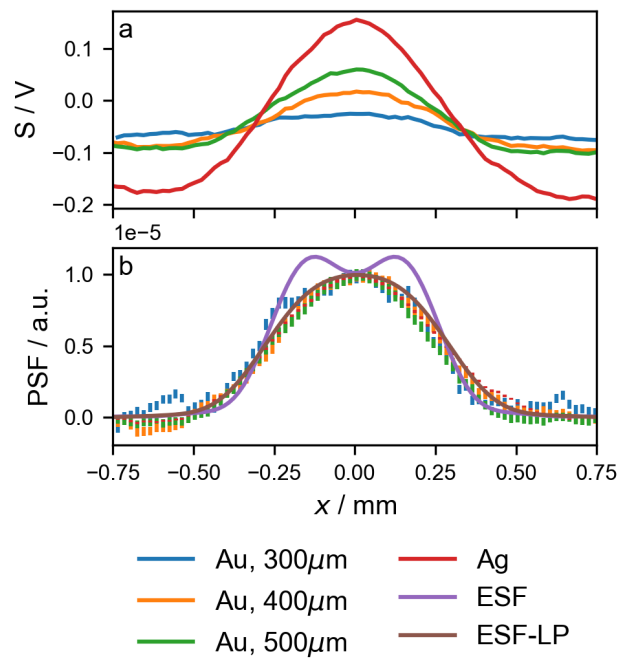


Figure S4: **a** Line scans collected at moderate speeds of gold (Au) and silver (Ag) disc targets. **b** Estimated PSFs using the scans from **a**, with a comparison to the PSF estimated from the ESF and the PSF with a 300  $\mu\text{m}$  low-pass filter.

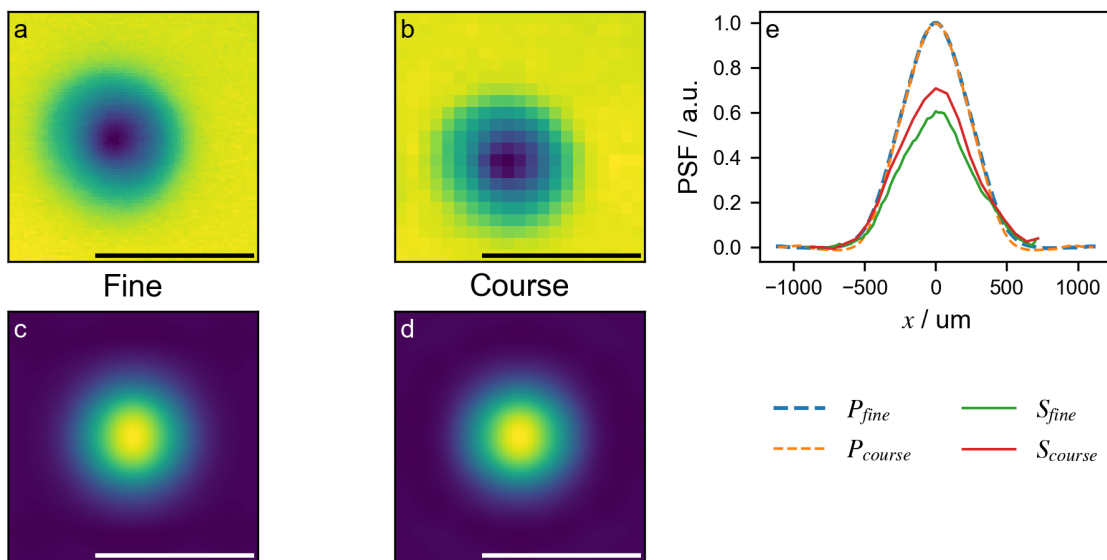


Figure S5: **a,b** Fine and course scans of a small disc-like target. **c,d** Estimated PSFs from the scan. **e** Slices through centre of scans comparing profiles for PSFs,  $P$ , and measured signal,  $S$ .

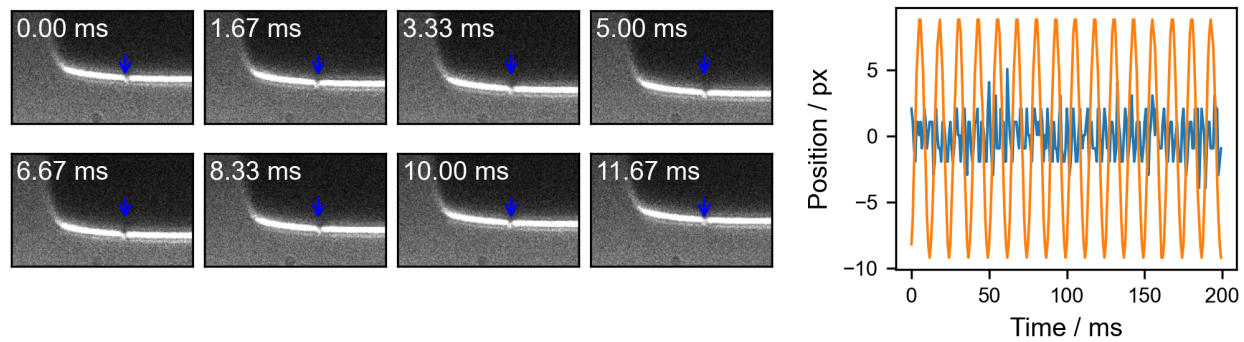


Figure S6: Still images and measured tip trajectory illustrating the motion of the tip. The arrow is meant as a visual guide, indicating a fixed reference spot in each image.